Gas-solid hydrodynamics in a stator-rotor vortex chamber reactor

Gas-solid hydrodynamics in a stator-rotor vortex chamber reactor

Xiaojun Lang [1], Yi Ouyang [1], Laurien A. Vandewalle [1], Bahman Goshayeshi [1], Siyuan Chen [1], Sepehr Madanikashani [1] , Patrice Perreault [2], Kevin M. Van Geem [1]* ,

[1] Ghent University, Laboratory for Chemical Technology, Technologiepark 125, 9052 Gent, Belgium.

[2] University of Antwerp, Faculty of Science, Institute for Environment and Sustainable Development (IMDO), Campus Groenenborger V.612, Groenenborgerlaan 171, 2020 Antwerpen.

*Corresponding author: Technologiepark 121, 9052 Gent, Belgium; Kevin.VanGeem@UGent.be

Abstract

The gas–solid vortex reactor (GSVR) has enormous process intensification potential. However the huge gas consumption can be a serious disadvantage for the GSVR in some applications such as fast pyrolysis. In this work, we demonstrate a recent novel design, where a stator-rotor vortex chamber (STARVOC) is driven by the fluid's kinetic energy, to decouple the solids bed rotation and gas. Gas-solid fluidization by using air and monosized aluminum balls was performed to investigate the hydrodynamics. A constructed fluidization flow regime map for a fixed solids loading of 100 g shows that the bed can only be fluidized for a rotation speed between 200 and 400 RPM. Below 200 RPM, particles settle down on the bottom plate and cannot form a stable bed due to inertia and friction. Above 400 RPM, the bed cannot be fluidized with superficial velocities up to 1.8 m/s (air flow rate of 90 Nm3/h). The bed thickness shows some non-uniformities, being smaller at the top of the bed than at the bottom counterpart. However by increasing the air flow rate or rotation speed the axial nonuniformity can be resolved. The bed pressure drop first increases with increasing gas flow rate and then levels off, showing similar characteristics as conventional fluidized beds. Theoretical pressure drops calculated from mathematical models such as Kao et al. model agree well with experimental measurements. Particle velocity discrepancies between the top and bottom particles reveal that the impact of gravity cannot be completely neglected. Design guidelines and possible applications for further development of STARVOC concept are proposed based on fundamental data provided in this work.

Keywords

Process intensification; Fluidization-defluidization cycle; Bed thickness; Pressure drop

1. Introduction

Process intensification (PI), as a promising tool to improve reactive and non-reactive processes by increasing volumetric productivity [1], [2], reducing energy consumption [3] and wastes [4], has attracted considerable interest in chemical and other energy intensive industries. For example extensive efforts have been devoted to enhance the performance of gas–solid contactors, resulting in the development of fluidized beds [5] to replace fixed bed reactors in many situations. However, the gas–solid slip velocity in conventional fluidized beds, which is a key driver for interphase heat and mass transfer, is restricted by the terminal velocity in gravitational fields [6]. To remove this limitation, one popular option is to replace the gravitational field with a centrifugal field [7], [8], [9], [10], [11], which allows to reach orders of magnitude higher slip velocities. The centrifugal force can be generated in different ways. For instance, a reactor vessel rotating around its axis of symmetry is driven by a motor, often this type of reactor is referred to as a rotating fluidized bed (RFB) [12], [13]. In an RFB, the rotation of particles is controlled by the motor power independently, which allows good flexibility of operating conditions. RFBs have been applied for various processes, such as drying [14], [15] and the production and coating of fine powder [16], [17], [18]. The main problems that limit the application of RFBs are mechanical vibration and wearing of seals due to the rotating vessels [19].

To circumvent this problem, the static gas–solid vortex reactor (GSVR) [6], [20] has been considered because of its ability to enhance various processes, for instance, drying [21], [22], [23], fast pyrolysis [24], [25], and SO2 and NOx adsorption [26], etc. This static device is inevitably mechanically simpler than RFBs. By introducing gas through a set of tangentially inclined slots in the circumferential wall, particles rotate after gaining momentum from gas, thus generating a centrifugal force that counteracts the gas–solid drag force. In a given GSVR, both the centrifugal force and drag force increases with increasing gas flow rate [10] in a wide gas flow range. A sufficiently high gas flow rate generates a strong bed rotation, and thus a high slip velocity. The GSVR has been investigated experimentally and numerically, proving its excellent characteristics in process intensification [6]. However, in addition to the reduced flexibility for operating a GSVR associated with the fact that bed rotation is driven by the gas flow, several other drawbacks are entrainment of particles (especially for fine particles) [27], relatively high carrier gas–solid mass ratio [21], and low azimuthal velocity due to particle–wall friction [11].

Inspired by the RFB and GSVR, an innovative stator-rotor vortex chamber (STARVOC) reactor has been recently developed and patented [28], [29]. In this reactor, a rotor with several angled blades inside a static cylindrical chamber is driven by tangential injection of gas. The rotor also functions as a gas distributor due to the presence of perforations on the outer wall to produce a vortex chamber in which

particles form a densely and uniformly bed. It has been demonstrated experimentally that the azimuthal velocities can be up to four-fold to that of the existing GSVR [28]. In addition, the use of gas kinetic energy to impart the angular momentum increases the energy efficiency [28]. To achieve an optimal design of this STARVOC technology, i.e. finding the optimal geometrical parameters of the chamber such as the diameter/length of the chamber and the number of blades, etc., hydrodynamic studies are essential. The hydrodynamic characterization allows to map the operation conditions (gas flow rate and rotation speed) under which the bed can be considered fluidized.

In this work, we present a prototype of a fully transparent vortex chamber reactor that aims to gain an understanding of gas–solid hydrodynamics by decoupling the gas flow rate and rotation speed. A fluidization flow regime map is established which indicates whether the fluidization occurs, based on visual inspection and pressure drop analysis. Then a parametric study is conducted to investigate the gas–solid flow behavior in the reactor. The influence of the gas flow rate, rotation speed and solids loading is discussed. In addition, the role of gravity in solids distribution and consequently the bed pressure drop and particle velocity is revealed. This hydrodynamic study obtained from this rotor reactor will allow improving the design of the next generation of a blade-driven reactor (STARVOC).

2. Experimental set-up and procedure

2.1 Experimental set-up

The experimental set-up as illustrated in Fig. 1, consists of an air supply, the STARVOC reactor and a solids separation section. Particulate solids are pre-weighed and fed into the reactor chamber manually. Compressed air (Atlas Copco, GA90VSD) is fed via a mass flow controller (Bronkhorst, F-106 CI). A cyclone (Volkmann, VS200) installed downstream is used to separate entrained solid particles from the air at the outlet. A photographic view of the experimental GSVR setup is shown in Fig. 2.

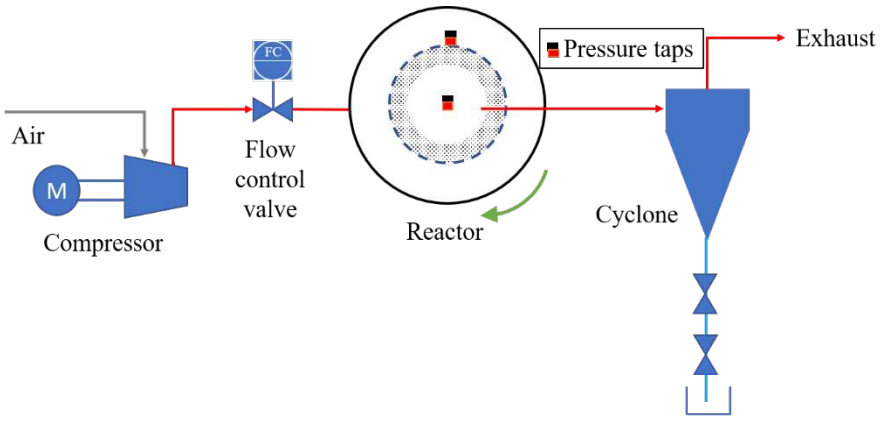

Fig. 1. Process flow diagram of the STARVOC unit.

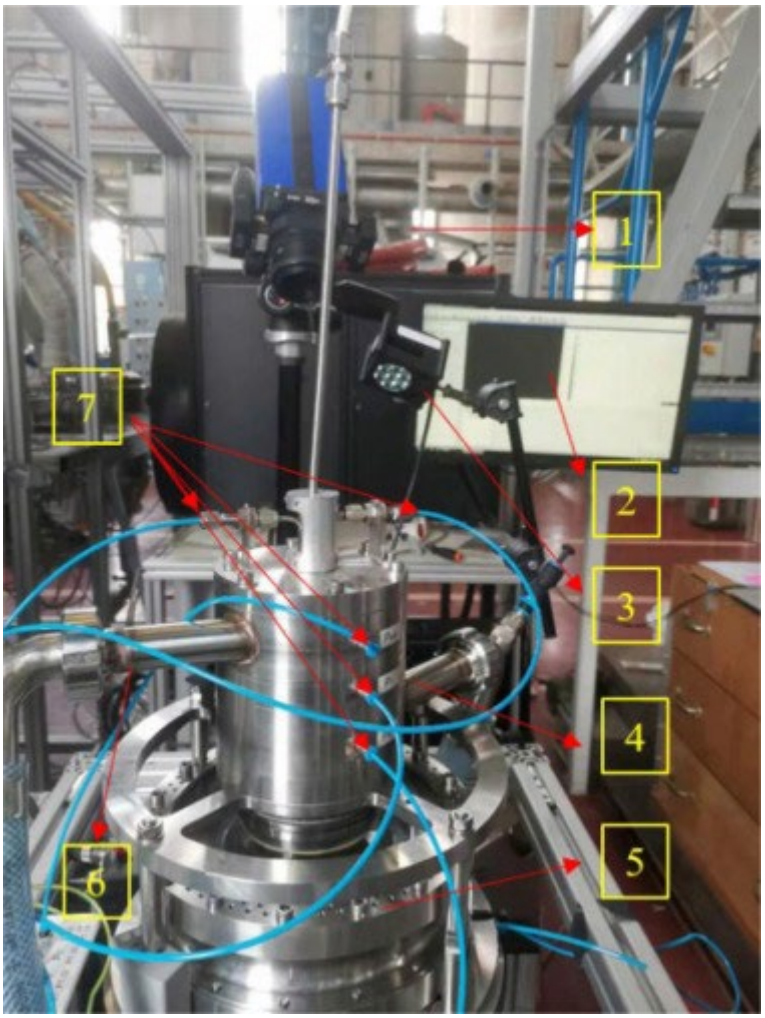

Fig. 2. Photographic view of the STARVOC unit. 1 - PIV camera, 2 - computer, 3 - light, 4 - air inlet, 5 - reactor, 6 - air outlet, 7 - pressure measurement taps.

The reactor (Fig. 3a) represents the central piece of the set-up which rotates around its vertical axis of symmetry. A variable speed electric motor (Simens, Simotics S-1FK7) can control the rotation around this vertical axis and makes sure that the rotation speed can be precisely set in a wide range of 0 ~ 1000 RPM. Note that the STARVOC does not include a motor but is freely rotating at an RPM defined by its design. However, for studying the hydrodynamics in this rotating device we have opted to include a motor to gain insight at very precise controlled RPMs. The gas distributor (Fig. 3b) consists of a circumferential cylindrical outer wall with 1400 equidistant inclined holes acting to distribute the gas. The distributor is positioned in between two transparent endplates. All these holes are arranged in a regular triangular pattern and have the same diameter of 1 mm, accounting for 9.72% opening. Table 1 summarizes the geometric properties of the gas distributor. Pressure taps placed in the reactor are connected to two differential pressure sensors (Druck, UNIK 5000). The pressure drops across the air inlet and the inner periphery of the gas distributor ($\Delta P1$), and across the air inlet and the center of the reactor ($\Delta P2$) are measured respectively, therefore the pressure drop across the particle bed is given by:

$$\Delta P = \Delta P2 - \Delta P1 \quad (1)$$

7

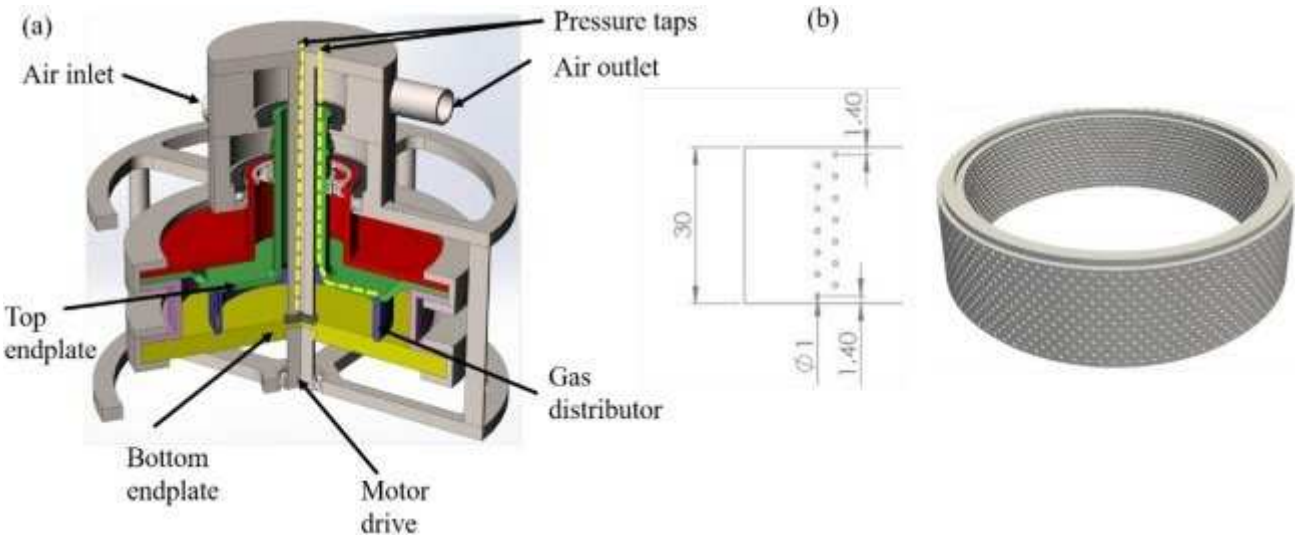

Fig. 3. a) Three-dimensional view of the reactor. Grey part is stainless steel, red, green and yellow parts are transparent polycarbonate. Two endplates and gas distributor are rotating. The two dashed lines represent small channels used to measure pressure. b) Gas distributor with equidistant holes. All holes have a 30° inclination. (For interpretation of the references to colour in this figure legend, the reader is referred to the web version of this article.)

Table 1. Detailed information of the gas distributor.

Parameter	Value
External diameter (m)	0.14
Internal diameter (m)	0.12
Height (m)	0.03
Holes diameter (m)	0.001
Holes inclination angle (°)	30
Number of jets	100×14
Opening (%)*	9.72

*Note: opening percentage is the ratio of the sum area of all holes to the distributor area based on internal diameter.

The rotation speed along with other data like the air flow rate and pressure drop are recorded online with a frequency of 4 Hz.

A charge coupled device (CCD) camera of 4 megapixels (Imager-ProX4M) is either above or below the reactor to record images used to visually inspect if the bed is fluidized, as well as for digital image processing and particle image velocimetry (PIV). For PIV, calibration is performed to convert the pixel size in distance by using a calibration plate printed with an equidistant dots matrix, placed directly on the inner side of the bottom endplate (or on the inner side of the top endplate). LaVision DaVis software 8.1.6 is used for synchronizing the camera and the reactor by setting the recording frequency the same as the rotation speed. A LED light (Rood, Multiled ST) is employed to illuminate particles when taking single-frame images. The images are pre-processed (background subtraction and time-average) via the DaVis software for further analysis. By importing the images to ImageJ (version 1.46r), we measure the bed thickness at five different azimuthal locations (Fig. 4). The inner radius of the solids bed is also calculated from image processing for pressure drop modeling.

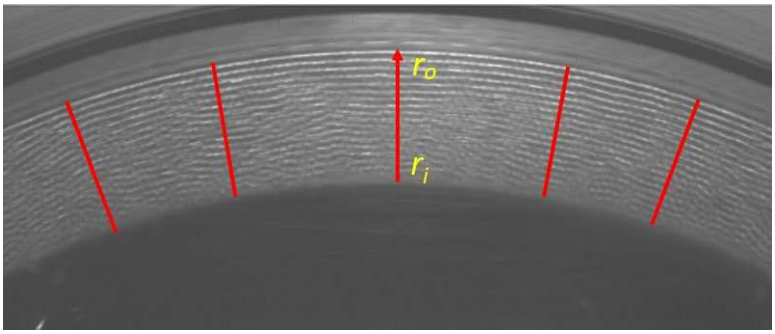

Fig. 4. Illustration of the ted thickness measured by ImageJ software. The length of red lines represents bed thickness. r_o and r_i are radius of the inner edge and outer edge of solids bed.

2.2 Experimental procedure and design

The experiments are conducted within the operating conditions given in Table 2. Each run of the experiment started by manually weighing and feeding monosized aluminum balls into the reactor chamber. The rotation speed of the rotor is then set to its setpoint. The rotation spreads the particles over the gas distributor due to the centrifugal force. After letting the particles get evenly distributed on the gas distributor, the gas flow rate was increased stepwise from 0 to 90 Nm3/h (superficial air velocity 0 ~ 1.8 m/s), then decreased back to 0, i.e., that we performed a conventional fluidization-defluidization cycle. For each air inlet flow rate, 100 single-frame images were recorded for measuring the bed thickness. The fluidization of the bed was tracked using a combination of visual inspection and pressure drop measurements.

Table 2. Overview of operating conditions for monosized aluminum balls.

Operating condition	Range
Air flow rate/(Nm3/h)	0 ~ 90
Superficial air velocity/(m/s)	0 ~ 1.8
Particle size/mm	0.5
Particle density/(kg/m3)	2700
Solids loading/g	100, 150, 200
Rotation speed/RPM	100, 200, 300, 400, 500

3. Results and discussion

3.1 Fluidization map

Solid particles in the reactor are subjected to the outward centrifugal force, inward gas–solid drag force, and downward gravitational force. For a rotating bed, fluidization is the result of the balance between the centrifugal force and the drag force. As the centrifugal force is proportional to the square of the rotational velocity, a strong centrifugal forces can be generated in the vortex reactor. To investigate the influence of the rotational velocity and the air flow rate on the flow behavior of aluminum balls, the solids loading of 100 g was fixed and the air flow rate increased gradually at a certain rotational velocity. The movement of particles was visually observed via the synchronized CCD camera. To better understand this, videos and images can be found in the Supplementary Information to show the solids bed under different operation conditions. With increasing air flow rate, the bed evolved from a fixed bed to a partially fluidized bed and eventually a full fluidized bed. This layer-by-layer fluidization has been investigated by Chen [7], and Kao et al [30], Qian et al [31]. The pressure drop across the bed was also recorded so that the fluidization regime is discerned. The bed pressure drop increases with increasing superficial air velocity until fluidization occurs, then remains almost unchanged. From the characteristics of the bed pressure drop, the corresponding fluidization flow regime map is established, as shown in Fig. 5.

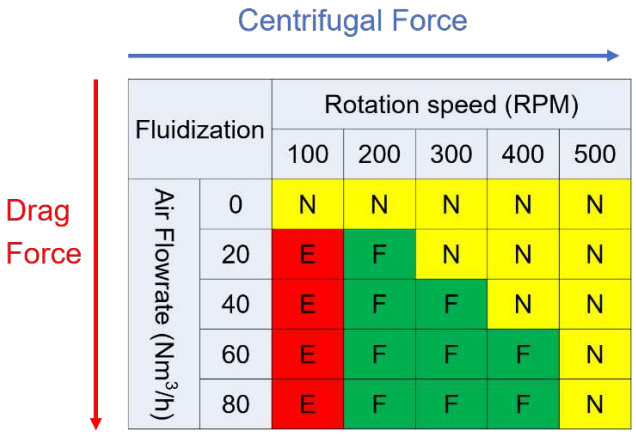

Fluidization		Rotation speed (RPM)				
		100	200	300	400	500
Air Flowrate (Nm^3/h)	0	N	N	N	N	N
	20	E	F	N	N	N
	40	E	F	F	N	N
	60	E	F	F	F	N
	80	E	F	F	F	N

Fig. 5. Fluidization map for aluminum balls at different combinations of air flow rates and rotation speeds (in which 'E' denotes entrainment which means remarkable entrainment occurred at the corresponding rotation speed and air flow rate, 'F' denotes fluidization which means particles were fluidized at the corresponding rotation speed and air flow rate, 'N' denotes no fluidization which means there was no fluidization at the corresponding rotation speed and air flow rate).

Fig. 5 shows that at a low rotation speed (e.g. 100 RPM), aluminum balls were easily entrained by the air and cannot form a stable bed. Nearly all particles settled down on the bottom endplate and only a few particles were dispersed on the gas distributor, indicating that the centrifugal force at low rotation speeds was not sufficient to counteract the inertial force and friction (particle–particle, particle–wall). Considering the air velocity increases with decreasing radius, particles were easily entrained when they were on the bottom endplate. On the other hand, when the rotation speed was high (e.g. 500 RPM), the particles bed was so densely packed that it cannot be fluidized even at the maximum air flow rate, which implies that the centrifugal force was stronger than the drag force. Overall, only for a limited range of rotational velocities fluidization can be observed. Between 21 ~ 42 rad/s (200 ~ 400 RPM), the transition between a rotating packed bed and a rotating fluidized bed occurred when the superficial air velocity increased gradually from 0 to 1.8 m/s (air flow rate from 0 to 90 Nm3/h).

It is worth mentioning that the flow behavior of particles from the top view and bottom view at the same operational conditions was different due to the gravity effect. The downward oriented gravity makes particles tend to accumulate on the bottom endplate, which results in axial nonuniformity of the bed. This will further be demonstrated by the results of bed thickness measurements in Section 3.2, in which the bottom bed thickness is always larger than the top bed thickness. Besides, the nonuniform distribution of particles over the gas distributor leads to a nonuniform distribution of the air through the bed as the flow resistance is not axially even. It is not surprising that incipient fluidization was first observed from the top view. For example, particles at the top of the bed began to move and vibrate at superficial air velocity around 0.98 m/s (40 Nm3/h) with the solids loading of 100 g and the rotation

speed of 300 RPM, while particles on the bottom endplate were still static with respect to the gas distributor. Therefore we can speculate that the incipient fluidization starts from the top then goes down to the bottom with increasing the air flow rate. Similarly, the intensity of particles movement is also axially different, and the particles of the upper part bed are more turbulent when the bed is in the fluidization regime.

Regarding the demarcation of fluidization regimes, conventional fluidized beds have been extensively studied. Many generalized correlations [32], [33] extracted from large experimental databases to differentiate fluidization regimes are available. These correlations are used to determine the boundaries between different fluidization regimes and consequently, fluidization maps can be constructed. However, the fluidized bed in STARVOC is different and could be regarded as similar to a rotating fluidized bed, in which particles are fluidized against the centrifugal force instead of gravitational force. The centrifugal force depends on the rotation speed, which is adjustable. This makes the rotating fluidized bed in STARVOC much more complicated in terms of differentiating fluidization regimes.

The fluidization regime map will remain the same regardless of the process of adding solids or whether the chamber is driven by the gas or a motor. The fluidization behavior of particles in STARVOC is determined by the rotation speed (centrifugal force) and the gas flow rate (drag force). It is worth mentioning for a chamber (motor-free) driven by gas, it might be difficult to achieve different fluidization regimes as the rotation speed and gas flow rate are coupled. This also explains why we have to carry out the present study, i.e., to explore the interesting combinations of the rotation speed and gas flow rate as many as possible by decoupling these two. In this way, we will obtain different flow behaviors, which is helpful for the future customization of STARVOC to meet different fluidization regimes. As for the impact of the startup process, it can be removed once all particles in the bed are fluidized. Also note that Geldart's particle classification based on the fluidization behavior agrees well with conventional fluidized beds. For a rotating fluidized bed in STARVOC, it is not the case. For example, type A particles can shift to type B under a strong centrifugal field [12]. Therefore, the boundary between different types moves when centrifugal acceleration changes. Simply put, compared with conventional fluidized beds, rotating fluidized beds have more flexibility (changing rotation speed) to alter the fluidization behavior of particles.

3.2 Bed thickness measurements

3.2.1 Start-up effect

To illustrate the start-up effect, we choose the combination of 100 g and 41.9 rad/s (400 RPM) as an example. Single-frame images recorded at each flow rate from the top view (and bottom view) were

used to measure the top (and bottom) bed thickness. The data corresponding to cycling up and cycling down air flow in the first loop is labeled as '1st loop - Ascending' and '1st loop- Descending' respectively, as shown in Fig. 6. Similarly, the data for the next cycles are labeled as '2nd loop- Ascending' and '2nd loop- Descending' and so on. Fig. 6 shows the comparison of the top bed thickness and bottom bed thickness as a function of the superficial air velocity (which is calculated using internal diameter of the gas distributor). The bed thickness profile in the first fluidization-defluidization cycle differs from the bed thickness profile obtained in all subsequent cycles, which is called the start-up effect in this study. This is related to the experimental procedure. The particles are poured into the static chamber and they form a heap at the center of the bottom endplate because of the particle–particle and particle–wall friction. Then the chamber starts to rotate by setting the rotation speed in the control system. Particles are pushed away from the center of the bottom endplate to the gas distributor due to the centrifugal force. In subsequent fluidization-defluidization cycles with the gas flow rate increasing and decreasing stepwise, the bed experienced expansion and contraction, during which particles adjust their positions and locations. From the experimental procedure we can see that in the first fluidization-defluidization cycle, particles need to be displaced in the centrifugal field. This is where the start-up effect comes from. Besides, that displacement is completed in the first cycle. In the rest cycles, there is no such displacement, the start-up effect disappears.

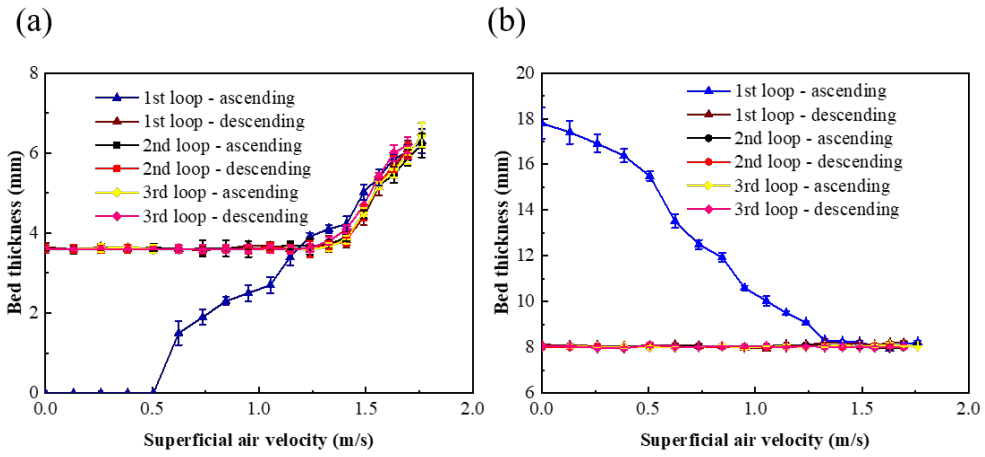

Fig. 6. Bed thickness for solids loading of 100 g and rotating speed of 42 rad/s (400 RPM) measured at top (a) and bottom (b) in 3 cycles of fluidization-defluidization. 'ascending' denotes increasing air flow rate to fluidize solids bed, 'descending' is the opposite.

For the top bed thickness, in the first loop when the superficial air velocity was lower than 0.51 m/s, the bed thickness was zero due to gravity. With increasing the air flow rate, particles started to move upward to the top endplate, the top bed thickness increased significantly. At the largest air flow rate, the top bed thickness achieved the peak value. When the air flow rate cycled down, at first the top bed thickness almost followed the same locus as that for air flow rate cycling up and then became relatively constant. With a further decrease in air flow rate, the top bed thickness remained unchanged. Even when the air

flow rate went back to 0 again, the top bed thickness did not return to zero. In the next loops, all the top bed thickness curves followed nearly the same locus as that for the first cycling down.

On the other hand, the bottom bed thickness contracted from its maximum value significantly when the air velocity increased gradually to around 1.33 m/s in the first loop. As the flow rate further increased, the bed thickness kept at a constant level. The interesting point is that after the bottom bed thickness shrank to the minimal value, it stayed unchanged no matter how the air flow rate cycled up or down. This is why the curves of the second loop overlapped with each other. However, the unchanged bed thickness does not suggest that particles movement was not influenced by the air flow rate. In fact, we observed from the camera that the relative movement of particles with respect to the gas distributor was enhanced slightly when the air flow rate increased and the particle velocity was dominated by its angular component.

3.2.2 Bed thickness profiles

Top and bottom bed thickness in the second loop for 20.9, 31.4 and 41.9 rad/s (200, 300 and 400 RPM) are presented in Fig. 7, Fig. 8, Fig. 9 respectively. In the cases of 200 g, a slight difference is that the bottom bed thickness did not remain constant after reaching the lowest level. It showed an upward trend once the air flow rate increased to a relatively high level. For instance, the bottom bed thickness for solids loading of 200 g and rotation speed of 31.4 rad/s (300 RPM) increased slightly when the air flow rate increased to 1.15 m/s. Moreover, compared with its 41.9 rad/s (400 RPM) counterpart, the upward trend is more pronounced.

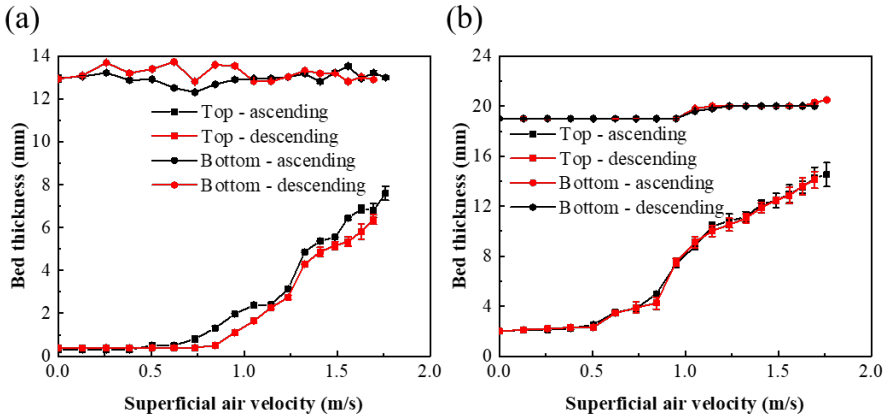

Fig. 7. Bed thickness profiles for 200 RPM with solids loading of (a) 100 g and (b) 150 g. 'ascending' denotes increasing air flow rate to fluidize solids bed, 'descending' is the opposite.

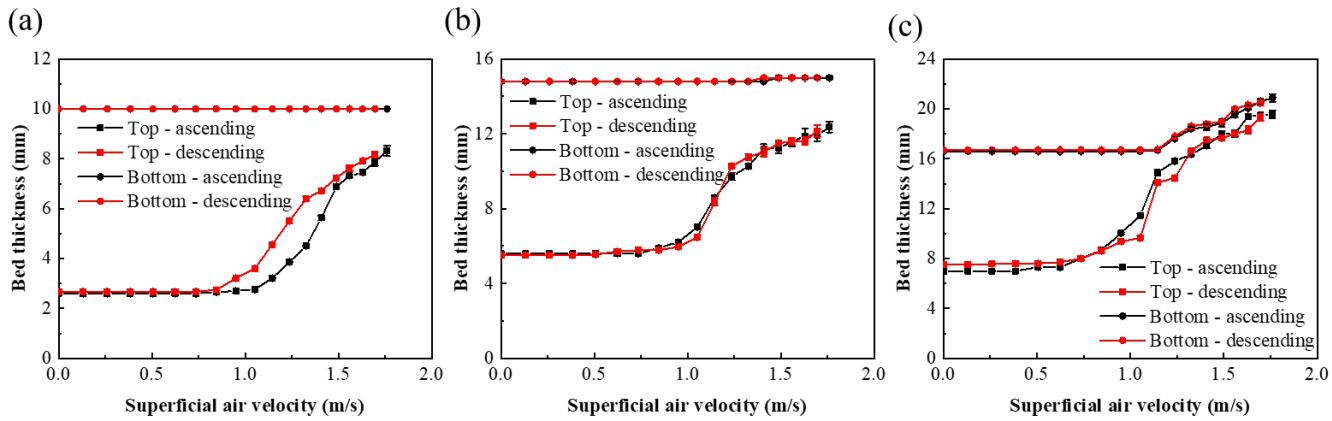

Fig. 8. Bed thickness profiles for 300 RPM with solids loading of (a) 100 g, (b) 150 g and (c) 200 g. 'ascending' denotes increasing air flow rate to fluidize solids bed, 'descending' is the opposite.

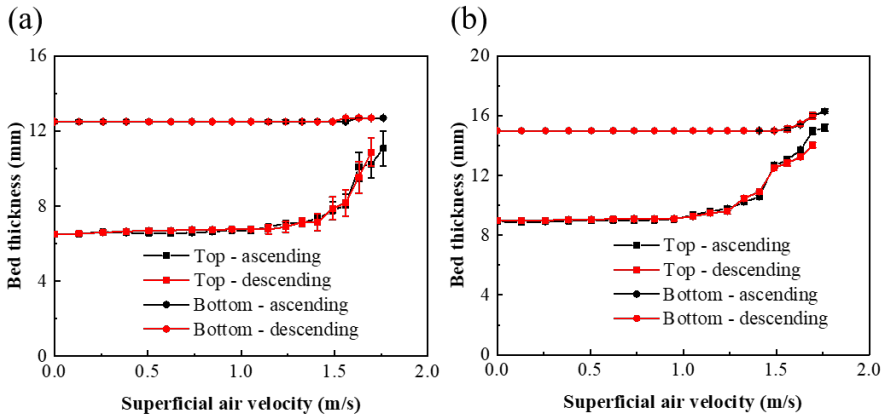

Fig. 9. Bed thickness profiles for 400 RPM with solids loading of (a) 150 g and (b) 200 g. 'ascending' denotes increasing air flow rate to fluidize solids bed, 'descending' is the opposite.

It is worth mentioning that the rotation speed has an obvious effect on the bed uniformity. With a relatively high rotation speed, e.g. 41.9 rad/s (400 RPM), we can achieve good uniformity of the rotation bed. In other words, the gravity effect is weakened at high rotation speeds. Overall, both the air flow rate and rotation speed influence the distribution of particles hence the shapes of the bed. The discrepancy between the top and bottom bed thickness can be reduced by increasing the air flow rate as well as the rotation speed. While the bed expansion is different, being more significant at the top of the solids bed. It should be noted that even if the bed is nonuniform with top bed thickness being roughly half of the bottom counterpart, all the solids in the reactor can be fluidized with a sufficiently high gas flow rate. Moreover, the variation of bed thickness in the axial direction is narrowed by increasing the gas flow rate. In this sense, all the solids account for effective loading.

3.2.3. Bed uniformity

The uniformity of rotating solids beds can be broken down into azimuthal uniformity and axial uniformity. In the present study, bed non-uniformities are primarily occurring in the vertical, i.e., axial direction as shown by the differences in top and bottom bed thickness. For simplicity, we use the angle

between the bottom endplate and the bed inner surface to describe axial bed uniformity in this study. Good axial uniformity corresponds to a larger bed inclination angle, indicating a smaller difference in the bed thickness at the top and the bottom. Note that the bed thickness measured at the top of the chamber is always smaller than the bottom counterpart. The bed uniformity or more general, the solids distribution, is the result of the force balance of the centrifugal force, drag force, gravity and interactions among particles. There are well-established equations or correlations [12], [34] to determine the first two forces. However, the interactions including collision among particles linked to the properties of particles, e.g. density, size, etc., are difficult to be determined. Even for certain particles (e.g. polycarbonate, glass beads) with low electrical conductivity, electrostatic charges buildup [35], [36] due to friction also plays a role in particle interactions. The downward gravity tends to settle particles down on the bottom endplate, which results in more particles at the bottom and fewer particles at the top, i.e., axial nonuniformity. A systematic investigation is needed to study the effect of particle types on azimuthal uniformity and axial uniformity, which will be addressed in future work.

In order to better illustrate how the axial uniformity is affected by the rotation speed, the inclination angle of the bed has been calculated. For simplicity, we assume the bed shape at the freeboard-bed interface to be similar to that of a liquid in rotation and the profile to be linear in the axial direction, as shown in Fig. 10. Kroger et al. [37] proposed the following equation to describe the distribution of particles in a rotating fluidized bed reactor, which can be used in this study. For a rotating fluidized bed in centrifugal fields, the angle formed between the bottom endplate and the inner bed surface is given by

$$\tan\theta = \frac{\omega r_m}{g} \qquad (2)$$

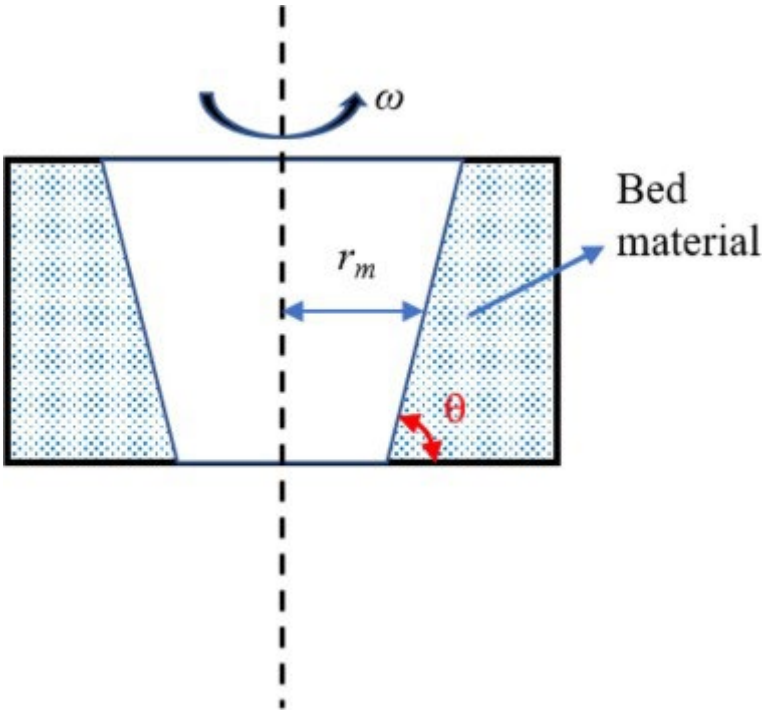

Fig. 10. The shape of rotating bed in STARVOC.

where θ is the bed inclination angle, ω is the angular velocity of particles, is the mean radius of the bed outer periphery, g is gravity acceleration.

First of all, from Eq. (2) we can see that improving the rotation speed can get a larger bed inclination angle, i.e., better bed uniformity. Theoretically the bed shape is unrelated to the properties of particles. While in reality solids particles are not free-flowing like a liquid. There are many factors that affect the flowability of particles. In addition to particle size and shape, it is also closely related to particle interaction forces, including friction and electrostatic interactions [12]. Besides the particles' properties, the above mentioned equation also does not take the bed expansion into consideration which also affects the bed shape. The bed thickness measurements reveal that the bed expansion in the axial direction is different when the gas flow rate is increased, with more expansion at the top and less at the bottom. Last but not least, the linear profile of solids bed at the gas–solid interface is valid only when the length to diameter ratios of reactor chambers is not very large. Otherwise, the profile has to be considered parabolic [37].

Here we present the bed inclination angles calculated from Eq. (2) based on bed thickness measurements. Increasing the rotation speed (centrifugal force) can diminish the gravity effect and consequently improve the axial bed uniformity. Table 3 shows that higher rotation speeds lead to larger bed inclination angles. Meanwhile, reducing solids loading is not very effective to overcome the axial

nonuniformity issue, which is also proved by the bed thickness measurements of different solids loading in the present study. At 400 RPM, the largest angle has been achieved is around 82°. It is interesting to be noted that the bed inclination angles calculated from Eq. (2) are always slightly larger than the experimental values under all operating conditions, which is caused by non-free flowing property of the particles. In other words, the particles tested in the present work are not as flowable as a liquid. Therefore, the distribution of particles, indicated by the inclination angles, is worse than the calculated results.

Table 3. Bed inclination angles at different operation conditions: experimental and calculated using Eq (2).

Rotation speed/RPM	Solids loading/g	Experimental bed inclination angle/°	Calculated bed inclination angle/°
200	100	67.1	67.3
	150	60.6	65.7
300	100	76.1	79.5
	150	72.9	78.7
	200	72.3	78.4
400	100	81.5	84.1
	150	78.7	83.7
	200	78.4	83.4

3.3 Bed pressure drop measurements

The pressure drop was first measured with no particles present in the reactor over the full air flow rate range, as shown in Fig. 11. A slightly higher pressure drop was obtained at a higher rotating speed. Besides, the pressure drop increased steadily to approximately 40 mbar with increasing air velocity to its maximum value.

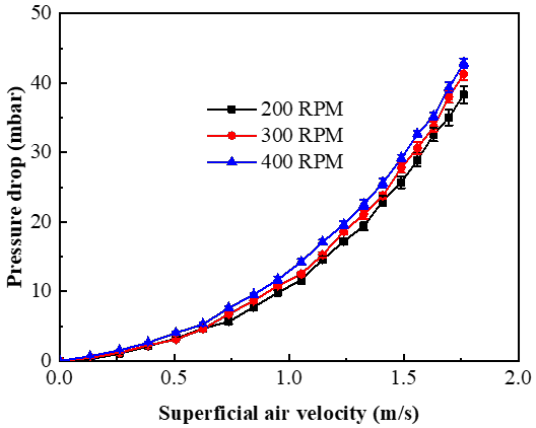

Fig. 11. Pressure drop for gas-only flow at 200, 300 and 400 RPM. A higher RPM causes a slightly higher pressure drop.

The pressure drop across the solids bed presented in Fig. 12, Fig. 13 is much smaller than that for gas-only flow in the full range of air flow rate. When no solids are present in the reactor, inclined injection of gas imparts a strong swirling motion to the gas and hence exhibits a flow pattern of a vortex, which causes a high pressure drop. When solids are loaded, the vortex is diminished remarkably due to the radial deflection of gas jets through the solids bed. This phenomenon has been previously observed experimentally and described as 'vortex suppression' by Kulkarni et. al. [38]. It is believed that a vortex forms inside the reactor regardless of the presence of particles. However, the vortex is small for gas–solid flows as the vortex is strongly suppressed as already demonstrated by De Wilde [6] and Kulkarni et al. [38]. This is why we did not exclude the pressure drop in the freeboard region caused by the vortex when measuring the (overall) bed pressure drop. Besides, the (overall) pressure drop across a rotating solids bed levels off after the bed is fluidized as demonstrated by Kao et al. [30], Qian et al. [31], Nakamura et al. [39], and Quevedo et al. [8]. In the present study, we observed the same phenomena. If the vortex would be significant, the (overall) pressure drop should keep on increasing with the increasing gas flow rate. As this is not the case, we can conclude that the impact of the vortex is negligible.

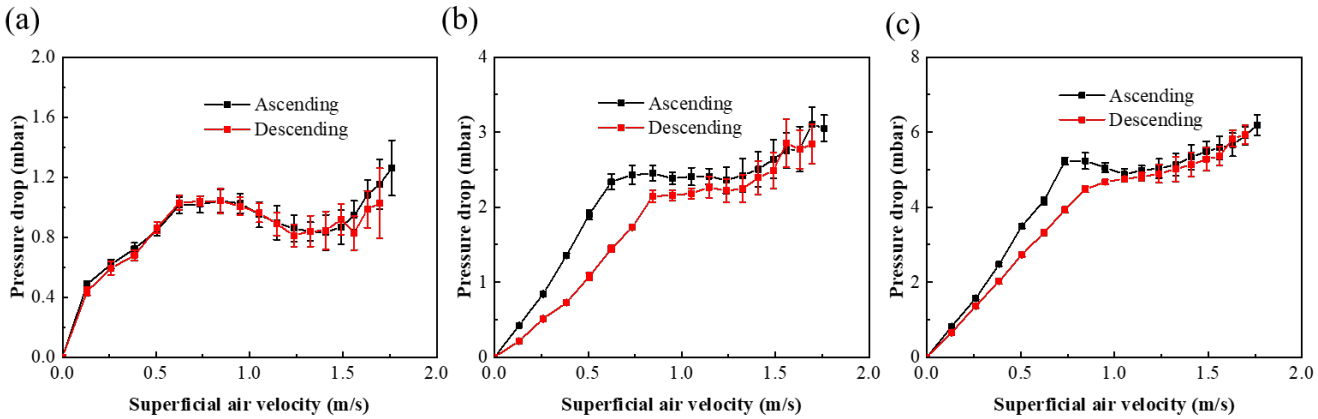

Fig. 12. Bed pressure drop for 300 RPM with solids loading of (a) 100 g, (b) 150 g and (c) 200 g. 'Ascending' denotes increasing air flow rate to fluidize solids bed, 'Descending' is the opposite.

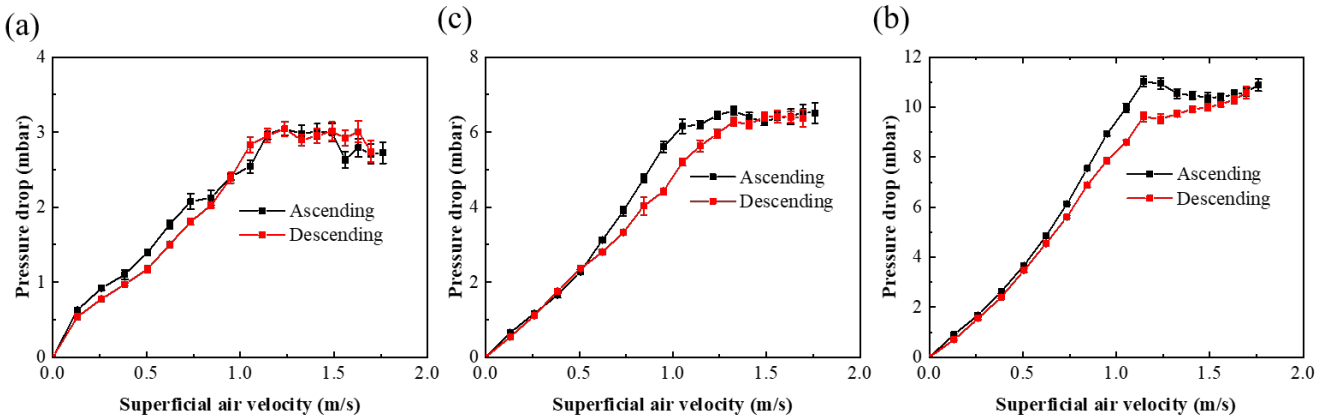

Fig. 13. Bed pressure drop for 400 RPM with solids loading of (a) 100 g, (b) 150 g and (c) 200 g. 'Ascending' denotes increasing air flow rate to fluidize solids bed, 'Descending' is the opposite.

Besides, the bed pressure drop profiles bear a strong resemblance to gravitational fluidized beds. The pressure drop increased nearly linearly with increasing air velocity until particles were fluidized and then leveled off with slight fluctuation or an upward trend. Each pressure drop curve exhibits a plateau which serves as an important indicator of fluidization. This is very useful to construct the fluidization map. Also, in general, the ascending pressure drop is slightly higher than the descending counterpart due to the hysteresis effect. By comparing the pressure drop at different solids loading, as expected, with a higher solids loading, there is a higher pressure drop. As discussed earlier, the rotating speed plays an important role in the axial uniformity of solids bed. Increasing the rotation speed can restructure the bed by weakening the gravity effect. Subsequently, the top bed thickness increases and the bottom bed thickness decreases. The pressure drop across the bed is more sensitive to the top bed thickness rather than its bottom counterpart as more gas flows through the upper part of the bed due to the lower flowing resistance. Therefore, in the packed bed regime with higher top bed thickness at higher rotation speeds, the bed pressure drop is increased. This can also be reflected by Eq. (4) in next section. According to Eq. (4), the bed pressure drop is determined by the particles' density, superficial air velocity, and bed surface radius . An increase in caused by higher rotation speed can increase the bed pressure drop.

3.4 Modeling of bed pressure drop

The bed pressure drop can also be estimated by the classical relations based on a theoretical model proposed by Kao et al. [1, 2]. In the packed bed regime, the pressure drop is given by

$$\frac{dP}{dr} = \emptyset_1\left(\frac{U_g r_0}{r}\right) + \emptyset_2\left(\frac{U_g r_0}{r}\right)^2 \quad (3)$$

In the fluidized bed regime, the pressure drop is given by

$$\frac{dP}{dr} = (\rho_p - \rho_g)(1-\varepsilon) r\omega^2 \tag{4}$$

where $\emptyset_1 = \frac{1650(1-\varepsilon)\mu}{d_p^2}$, $\emptyset_2 = \frac{24.5(1-\varepsilon)\rho_g}{d_p}$, U_g is the superficial air velocity, μ is the gas viscosity, ε is the bed voidage, ρ_g is the gas density, ρ_p is the particle density, ω is the angular velocity of particles, r_0 is the radius of the bed outer periphery (equals to the half of the inner diameter of the gas distributor) and r is the radial position. μ and ρ_g are considered for ambient conditions, that is 1.8×10^{-5} Pa·s and 1.225 kg/m^3 respectively.

Integrating Eqs. (3) and (4) gives the pressure drop in the packed bed regime

$$\Delta P = \emptyset_1 U_g r_o \ln\left(\frac{r_o}{r_i}\right) + \emptyset_2 \left(U_g r_o\right)^2 \left(\frac{1}{r_i} - \frac{1}{r_o}\right) \tag{5}$$

the pressure drop in the fluidized bed regime

$$\Delta P = \frac{1}{2}(\rho_p - \rho_g)(1-\varepsilon)\omega^2 (r_o^2 - r_i^2) \tag{6}$$

where r_i is the radial distance of the bed surface to the reactor center.

From Eqs. (5), (6) we can see that there are three important parameters, i.e. azimuthal velocity of particles , bed voidage and the radial position of the bed surface ri, which govern the calculation. For the sake of simplicity, the rotation speed of the chamber instead of the angular velocity of particles was used given that the relative velocity of particles with respect to the gas distributor is pretty small (see discussion in Section 3.5). Assuming a linear bed profile, the volume of the 3D trapezoidal bed can be calculated. The volume of solids added to the bed is the ratio of bed weight to the solids density. Given the bed volume and solids volume, an average bed voidage can be estimated. Either the top bed thickness or bottom bed thickness (even the average of the two) can be applied, however, we find that the pressure drop calculated by using bottom bed thickness is much higher than the experimental data. Therefore, the top bed thickness was chosen. In addition, only the second ascending up data was selected to make a comparison with the theoretically calculated data, as shown in Fig. 14, Fig. 15. The calculated pressure drop across the bed increases with increasing air velocity until the minimum fluidization velocity is reached then it becomes constant. The constant pressure is determined by the rotation speed and solids loading as indicated in Eq.(6). In general, the theoretical curves agree reasonably well with the experimental curves in the rotating packed bed regime while the pressure drop is being overpredicted in the fluidized bed regime. The smaller deviation from modeling for 400 RPM cases again demonstrates better axial uniformity compared with their 300 RPM counterparts. This matches the findings of the bed thickness measurements in which better bed uniformity is achieved at 400 RPM. Again, it reflects that the gravity effect can be minimized by employing high rotation speeds.

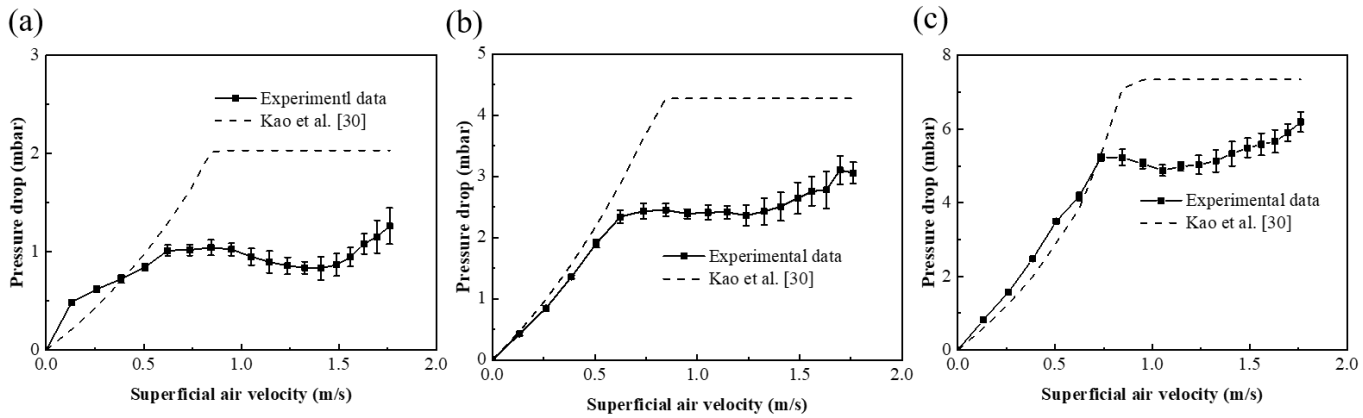

Fig. 14. Comparison of experimental and calculated pressure drop for 300 RPM with solids loading of (a) 100 g, (b) 150 g and (c) 200 g. dot - experimental data point, dash line – modeling value.

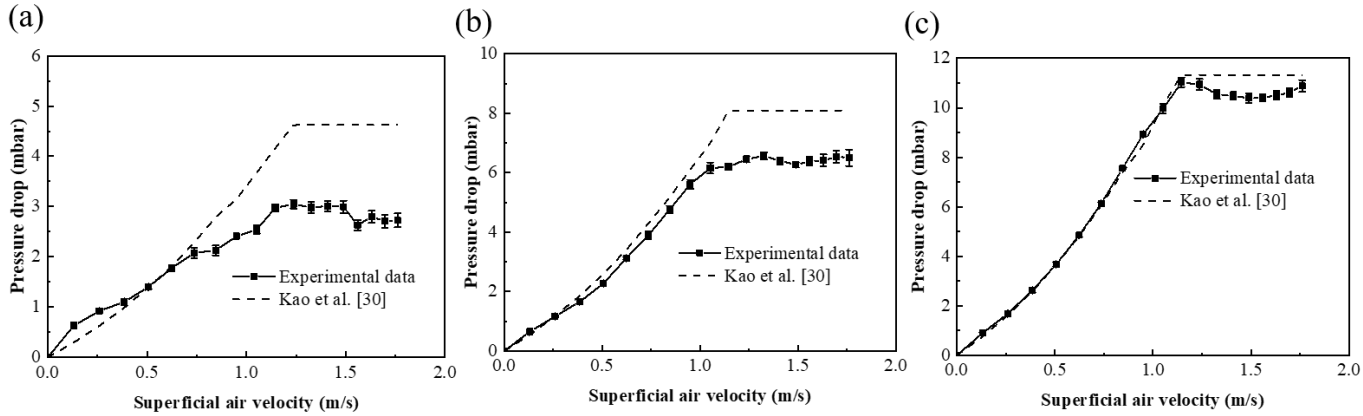

Fig. 15. Comparison of experimental and calculated pressure drop for 400 RPM with solids loading of (a) 100 g, (b) 150 g and (c) 200 g. dot - experimental data point, dash line - modeling value.

.

3.5 Particle velocity measurements

The movement of particles at the top visually observed by the camera is more turbulent than their bottom counterpart. In this section, we present the particle velocity measured at the top and bottom of the reactor which was obtained with 2D standard particle image velocimetry (PIV). To record double-frame images, the LED light source was replaced by a double-pulsed diffused laser light (135 mJ, 15 Hz, Nd:YAG Litron laser). 200 double-frame images were recorded and processed by LaVision DaVis software 8.1.6 to obtain particle velocity fields. Further details on the use of 2D PIV are described by Kovacevic et al [40]. Here we pick the representative results measured at the solids loading of 100 g. Fig. 16 summarizes both the particle velocity distribution measured at the top and the bottom of the chamber at 200 RPM with three different air velocities, i.e. 1.15 m/s, 1.49 m/s and 1.76 m/s (corresponding to 50 Nm3/h, 70 Nm3/h and 90 Nm3/h). The radial position of particles is defined as the distance between particles and the center of the top or bottom endplate. First of all, as expected the particle velocities at the top are always larger than the bottom due to the gravity effect. The largest relative velocity of particles with

respect to the gas distributor achieved at the top is around 0.7 m/s at the maximum air velocity. Fig. 17 shows the velocity profiles for 300 RPM and 400 RPM at the maximum air flow rate. Similarly, particle velocities at the top exceed the bottom counterpart. The difference is that the relative velocity is lower compared with 200 RPM results, indicating much less turbulent movement of particles at higher rotation speed. Overall, the increase in particle velocity attributed to an increase in air flow rate is sensitive to the rotation speed.

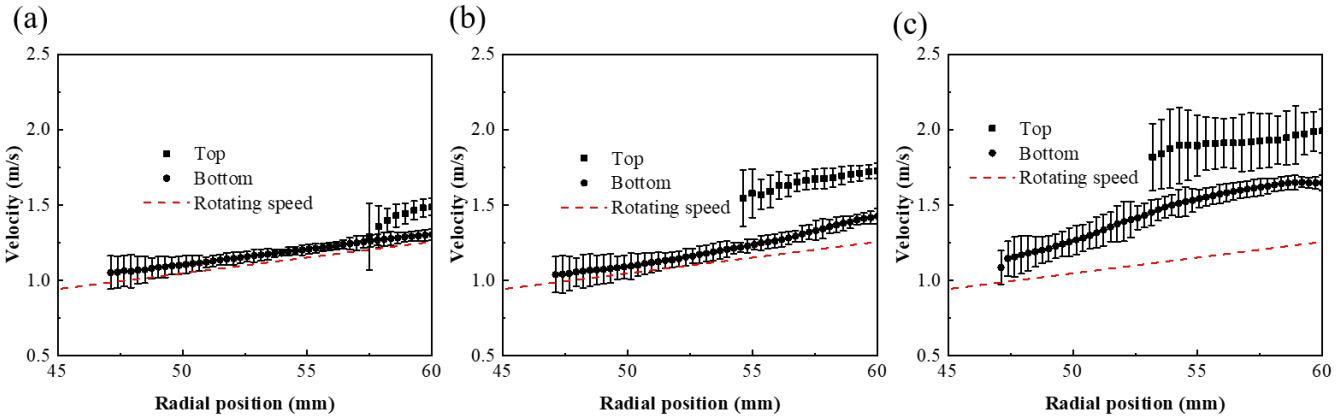

Fig. 16. Particle velocity profiles at top and bottom across the bed for 200RPM with three different air velocities: (a) 1.15 m/s; (b) 1.49 m/s; (c) 1.1.76 m/s. square - top particles, dot - bottom particles, dash line - rotating speed of motor.

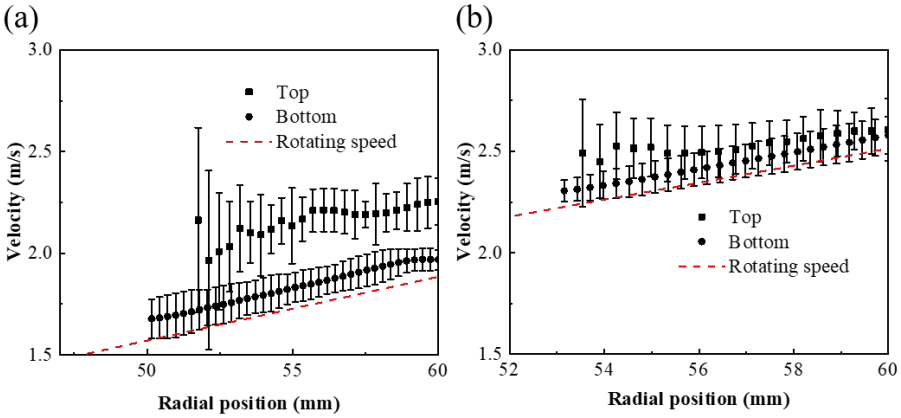

Fig. 17. Particle velocity profiles at top and bottom across the bed for (a) 300 RPM and (b) 400 RPM at the largest superficial air velocity. square - top particles, dot - bottom particles, dash line - rotating speed of motor.

3.6. Design guidelines and outlook for the STARVOC

The main advantages of the STARVOC compared to a static GSVR are the improved solids loading and reduced gas consumption. Although the bed is nonuniform in the axial direction with top bed thickness being roughly half of the bottom counterpart, all the solids in the reactor can be fluidized with a

sufficiently high gas flow rate. The variation of bed thickness in the axial direction is reduced by increasing the gas flow rate. In this sense, all the solids account for effective loading. Besides, the maximum solids loading of a GSVR with equivalent size to the STARVOC reactor is 46 ~ 66 g, which is estimated by Friedle et al. model [41]. Compared with its GSVR counterpart, the maximum solids loading of STARVOC is around four times higher. Meanwhile as the centrifugal force is generated mainly by the chamber rotation instead of the gas flow, the consumption of gas is dramatically reduced. The remarkable decrease in gas/solids mass ratio makes the STARVOC more commercially viable for applications where the gas is not a reactant. The fundamental understanding of gas–solid fluidization from this work can offer some guidelines for the design and further scale-up of the STARVOC concept. Firstly, the rotor of the STARVOC should be designed in a way such that the gas flow and the chamber rotation are matching to ensure that particles are fluidized without being entrained away from the chamber. Next, the rotation speed of the chamber should be sufficiently high to minimize the gravity effect to secure a uniform bed. Since the solids loading is determined by the balance of the centrifugal force and the drag force (gas flow rate), it is clear that by optimizing the chamber a high solids capacity can be achieved. Furthermore, as the gas distribution also affects the bed uniformity, a good design gas distributor is required to ensure uniform beds. STARVOC not only can be used for batchwise processes, but it is also possible to be applied to continuous processes which are more attractive for industrial applications. Besides the guidelines mentioned above, special attention should be paid to the design of the solids inlet and outlet to make sure that particles can be easily charged and discharged.

The STARVOC is still a new concept, further exploration of process intensification brought about by this novel design remains to be done. For instance, topics including a detailed study of fluidization behavior of various particles to establish the criteria to differentiate fluidization regimes, mathematical models developed to predict the maximum solids loading, and even controlled experiments with a motor-free STARVOC might be of most interest. To summarize, the STARVOC is a promising type of reactor which has exhibits some excellent characteristics, much experimental and numerical work, e.g. remained to be done to further optimize the design of STARVOC. A motor-free STARVOC will be designed and constructed based on the hydrodynamic data we gained in the present study so that we can assess the process intensification in various processes, e.g. drying, biomass pyrolysis, etc.

4. Conclusions

A parametric study was conducted to investigate gas–solid fluidization in a stator-rotor vortex chamber reactor. By using monosized aluminum balls as the bed material and air as the fluidizing agent, a fluidization map was constructed. The bed thickness was measured at the top and bottom separately. Due to the gravity effect, the bottom bed thickness is always larger than the top bed thickness, resulting in the axial nonuniform distribution of air. The bed inclination angle is used as an indicator to

quantitatively assess the axial uniformity of the bed under different operational conditions. With higher rotation speeds, better axial uniformity is achieved. The pressure drop across the bed levels off after entering the fluidized bed regime, which is similar to the one observed for conventional fluidized beds. The experimental data are fitted with theoretical models, showing good agreement in the rotating packed bed regime and overprediction in the fluidized bed regime. PIV measurements reveal that the particle velocity at the top exceeds the one at the bottom counterpart, further indicating the role of gravity in gas–solid hydrodynamics. Ultimately, the insights obtained in the motor-driven vortex chamber will be used to optimize the design of a free rotating blade-driven vortex chamber, i.e., STARVOC to overcome some of the disadvantages of the static GSVR.

Acknowledgement

The authors gratefully acknowledge financial support from China Scholarship Council (CSC). Yi Ouyang gratefully acknowledges financial support from the postdoctoral fellowship from the Research Foundation – Flanders (FWO) grant number 1273421N. Sepehr Madanikashani would like to acknowledge the support received from the European Regional Development Fund (ERDF) via the PSYCHE project (Interreg France-Wallonie-Vlaanderen) with co-financing from the provinces of East-Flanders and West-Flanders. This work was performed in the framework of the OPTIMA project (Grant Agreement No. 818607).

Reference

[1]

A.I. Stankiewicz, J.A. Moulijn

Process intensification: transforming chemical engineering

Chem. Eng. Prog., 96 (1) (2000), pp. 22-34, 10.1016/j.cep.2008.07.011

View PDFGoogle Scholar

[2]

H. Freund, K. Sundmacher

Towards a methodology for the systematic analysis and design of efficient chemical processes: Part 1. From unit operations to elementary process functions

Chem. Eng. Process. Process Intensif., 47 (12) (2008), pp. 2051-2060, 10.1016/j.cep.2008.07.011

ArticleDownload PDFView Record in ScopusGoogle Scholar

[3]

P. Lutze, D.K. Babi, J.M. Woodley, R. Gani

Phenomena based methodology for process synthesis incorporating process intensification

Ind. Eng. Chem. Res., 52 (22) (2013), pp. 7127-7144, 10.1021/ie302513y

View PDFView Record in ScopusGoogle Scholar

[4]

T. Van Gerven, A. Stankiewicz

Structure, energy, synergy, time - the fundamentals of process intensification

Ind. Eng. Chem. Res., 48 (5) (2009), pp. 2465-2474, 10.1021/ie801501y

View PDFView Record in ScopusGoogle Scholar

[5]

D. Kunii, O. Levenspiel, Fluidization Engineering, Butterworth-Heinemann 1991. doi: 10.1016/C2009-0-24190-0.

Google Scholar

[6]

J. De Wilde

Gas–solid fluidized beds in vortex chambers

Chem. Eng. Process. Process Intensif., 85 (2014), pp. 256-290, 10.1016/j.cep.2014.08.013

ArticleDownload PDFView Record in ScopusGoogle Scholar

[7]

Y.M. Chen

Fundamentals of a centrifugal fluidized bed

AIChE J., 33 (5) (1987), pp. 722-728, 10.1002/aic.690330504

View PDFView Record in ScopusGoogle Scholar

[8]

J. Quevedo, R. Pfeffer, Y. Shen, R. Dave, H. Nakamura, S. Watano

Fluidization of nanoagglomerates in a rotating fluidized bed

AIChE J., 52 (7) (2006), pp. 2401-2412, 10.1002/aic.10826

View PDFView Record in ScopusGoogle Scholar

[9]

G.H. Qian, I. Bágyi, R. Pfeffer, H. Shaw, J.G. Stevens

Particle mixing in rotating fluidized beds: inferences about the fluidized state

AIChE J., 45 (7) (1999), pp. 1401-1410, 10.1002/aic.690450705

View PDFView Record in ScopusGoogle Scholar

[10]

A. Gonzalez-Quiroga, P.A. Reyniers, S.R. Kulkarni, M.M. Torregrosa, P. Perreault, G.J. Heynderickx, K.M. Van Geem, G.B. Marin

Design and cold flow testing of a gas-solid vortex reactor demonstration unit for biomass fast pyrolysis

Chem. Eng. J., 329 (2017), pp. 198-210, 10.1016/j.cej.2017.06.003

ArticleDownload PDFView Record in ScopusGoogle Scholar

[11]

A. Gonzalez-Quiroga, S.R. Kulkarni, L. Vandewalle, P. Perreault, C. Goel, G.J. Heynderickx, K.M. Van Geem, G.B. Marin

Azimuthal and radial flow patterns of 1g-Geldart B-type particles in a gas-solid vortex reactor

Powder Technol., 354 (2019), pp. 410-422, 10.1016/j.powtec.2019.06.015

ArticleDownload PDFView Record in ScopusGoogle Scholar

[12]

G.H. Qian, I. Bágyi, I.W. Burdick, R. Pfeffer, H. Shaw, J.G. Stevens

Gas–solid fluidization in a centrifugal field

AIChE J., 47 (5) (2001), pp. 1022-1034, 10.1002/aic.690470509

View PDFView Record in ScopusGoogle Scholar

[13]

H. Nakamura, S. Watano

Numerical modeling of particle fluidization behavior in a rotating fluidized bed

Powder Technol., 171 (2) (2007), pp. 106-117, 10.1016/j.powtec.2006.08.021

ArticleDownload PDFView Record in ScopusGoogle Scholar

[14]

M. Shi, H. Wang, Y. Hao

Experimental investigation of the heat and mass transfer in a centrifugal fluidized bed dryer

Chem. Eng. J., 78 (2–3) (2000), pp. 107-113, 10.1016/S1385-8947(00)00148-0

ArticleDownload PDFView Record in ScopusGoogle Scholar

[15]

R. Carlson, R. Roberts, D. Farkas

Preparation of quick-cooking rice products using a centrifugal fluidized bed

J. Food Sci., 41 (5) (1976), pp. 1177-1179, 10.1111/j.1365-2621.1976.tb14411.x

View PDFView Record in ScopusGoogle Scholar

[16]

S. Watano, Y. Imada, K. Hamada, Y. Wakamatsu, Y. Tanabe, R.N. Dave, R. Pfeffer

Microgranulation of fine powders by a novel rotating fluidized bed granulator

Powder Technol., 131 (2–3) (2003), pp. 250-255, 10.1016/S0032-5910(03)00007-X

ArticleDownload PDFView Record in ScopusGoogle Scholar

[17]

S. Watano, H. Nakamura, K. Hamada, Y. Wakamatsu, Y. Tanabe, R.N. Dave, R. Pfeffer

Fine particle coating by a novel rotating fluidized bed coater

Powder Technol., 141 (3) (2004), pp. 172-176, 10.1016/j.powtec.2003.03.001

ArticleDownload PDFView Record in ScopusGoogle Scholar

[18]

H. Nakamura, N. Deguchi, S. Watano

Development of tapered rotating fluidized bed granulator for increasing yield of granules

Adv. Powder Technol., 26 (2) (2015), pp. 494-499, 10.1016/j.apt.2014.12.003

ArticleDownload PDFView Record in ScopusGoogle Scholar

[19]

J. Kovacevic, M. Pantzali, G. Heynderickx, G. Marin

Bed stability and maximum solids capacity in a gas–solid vortex reactor: experimental study

Chem. Eng. Sci., 106 (2014), pp. 293-303, 10.1016/j.ces.2013.11.018

ArticleDownload PDFView Record in ScopusGoogle Scholar

[20]

A.O. Kuzmin

Confined multiphase swirled flows in chemical engineering

Rev. Chem. Eng., 37 (1) (2021), pp. 31-68, 10.1515/revce-2019-0019

View PDFView Record in ScopusGoogle Scholar

[21]

P. Eliaers, J. De Wilde

Drying of biomass particles: Experimental study and comparison of the performance of a conventional fluidized bed and a rotating fluidized bed in a static geometry

Drying Technol., 31 (2) (2013), pp. 236-245, 10.1080/07373937.2012.726304

View PDFView Record in ScopusGoogle Scholar

[22]

P. Singh, P. Mahanta, P. Kalita

A comparative analysis and scale-up of a novel slit-less gas-solid vortex reactor dryer with spiral chimney versus conical chimney outlet

Int. Commun. Heat Mass Transfer, 121 (2021), Article 105112, 10.1016/j.icheatmasstransfer.2021.105112

ArticleDownload PDFView Record in ScopusGoogle Scholar

[23]

P. Singh, P. Kalita, P. Mahanta

Experimental study of food grain drying in a gas–solid vortex reactor

Drying Technol., 40 (5) (2022), pp. 884-896

View PDFCrossRefView Record in ScopusGoogle Scholar

[24]

M.N. Manzano, A.G. Quiroga, P. Perreault, S. Madanikashani, L.A. Vandewalle, G.B. Marin, G.J. Heynderickx, K.M. Van Geem

Biomass fast pyrolysis in an innovative gas-solid vortex reactor: Experimental proof of concept

J. Anal. Appl. Pyrol., 156 (2021), Article 105165, 10.1016/j.jaap.2021.105165

View PDFGoogle Scholar

[25]

R.W. Ashcraft, G.J. Heynderickx, G.B. Marin

Modeling fast biomass pyrolysis in a gas–solid vortex reactor

Chem. Eng. J., 207 (2012), pp. 195-208, 10.1016/j.cej.2012.06.048

ArticleDownload PDFView Record in ScopusGoogle Scholar

[26]

R.W. Ashcraft, J. Kovacevic, G.J. Heynderickx, G.B. Marin

Assessment of a gas-solid vortex reactor for SO2/NOx adsorption from flue gas

Ind. Eng. Chem. Res., 52 (2) (2013), pp. 861-875, 10.1021/ie300399w

View PDFView Record in ScopusGoogle Scholar

[27]

L.A. Vandewalle, A. Gonzalez-Quiroga, P. Perreault, K.M. Van Geem, G.B. Marin

Process intensification in a gas-solid vortex unit: computational fluid dynamics model based analysis and design

Ind. Eng. Chem. Res., 58 (28) (2019), pp. 12751-12765, 10.1021/acs.iecr.9b01566

View PDFView Record in ScopusGoogle Scholar

[28]

A. Gonzalez-Quiroga, V. Shtern, P. Perreault, L. Vandewalle, G.B. Marin, K.M. Van Geem

Intensifying mass and heat transfer using a high-g stator-rotor vortex chamber

Chem. Eng. Process. Process Intensif., 169 (2021), Article 108638, 10.1016/j.cep.2021.108638

ArticleDownload PDFView Record in ScopusGoogle Scholar

[29]

K.M. Van Geem, A. Gonzalez-Quiroga, G. Marin, V. Shtern, M. Pantzali

Stator-rotor vortex chamber for mass and/or heat transfer processes

Google Patents (2020)

Google Scholar

[30]

J. Kao, R. Pfeffer, G. Tardos

On partial fluidization in rotating fluidized beds

AIChE J., 33 (5) (1987), pp. 858-861, 10.1002/aic.690330520

View PDFView Record in ScopusGoogle Scholar

[31]

G.-H. Qian, I. Bágyi, R. Pfeffer, H. Shaw, J.G. Stevens

A parametric study of a horizontal rotating fluidized bed using slotted and sintered metal cylindrical gas distributors

Powder Technol., 100 (2–3) (1998), pp. 190-199, 10.1016/S0032-5910(98)00140-5

ArticleDownload PDFView Record in ScopusGoogle Scholar

[32]

Y. Makkawi, P. Wright

Fluidization regimes in a conventional fluidized bed characterized by means of electrical capacitance tomography

Chem. Eng. Sci., 57 (13) (2002), pp. 2411-2437, 10.1016/S0009-2509(02)00138-0

ArticleDownload PDFView Record in ScopusGoogle Scholar

[33]

H. Bi, J. Grace

Flow regime diagrams for gas-solid fluidization and upward transport

Int. J. Multiph. Flow, 21 (6) (1995), pp. 1229-1236, 10.1016/0301-9322(95)00037-X

ArticleDownload PDFView Record in ScopusGoogle Scholar

[34]

R. Chevray, Y.N.I. Chan, F.B. Hill

Dynamics of bubbles and entrained particles in the rotating fluidized bed

AIChE J., 26 (3) (1980), pp. 390-398, 10.1002/aic.690260310

View PDFView Record in ScopusGoogle Scholar

[35]

A.V. Patil, E. Peters, V.S. Sutkar, N. Deen, J. Kuipers

A study of heat transfer in fluidized beds using an integrated DIA/PIV/IR technique

Chem. Eng. J., 259 (2015), pp. 90-106, 10.1016/j.cej.2014.07.107

ArticleDownload PDFView Record in ScopusGoogle Scholar

[36]

J. Štěpek, H. Daoust

Antistatic Agents, Additives for Plastics, Springer New York, New York, NY (1983), pp. 124-134

View PDFCrossRefView Record in ScopusGoogle Scholar

[37]

D. Kroger, E. Levy, J. Chen

Flow characteristics in packed and fluidized rotating beds

Powder Technol., 24 (1) (1979), pp. 9-18, 10.1016/0032-5910(79)80002-9

ArticleDownload PDFView Record in ScopusGoogle Scholar

[38]

S.R. Kulkarni, A. Gonzalez-Quiroga, M. Nuñez, C. Schuerewegen, P. Perreault, C. Goel, G.J. Heynderickx, K.M. Van Geem, G.B. Marin

An experimental and numerical study of the suppression of jets, counterflow, and backflow in vortex units

AIChE J., 65 (8) (2019), p. e16614

View Record in ScopusGoogle Scholar

[39]

H. Nakamura, S. Watano

Fundamental particle fluidization behavior and handling of nano-particles in a rotating fluidized bed

Powder Technol., 183 (3) (2008), pp. 324-332, 10.1016/j.powtec.2008.01.007

ArticleDownload PDFView Record in ScopusGoogle Scholar

[40]

J.Z. Kovacevic, M.N. Pantzali, K. Niyogi, N.G. Deen, G.J. Heynderickx, G.B. Marin

Solids velocity fields in a cold-flow gas–solid vortex reactor

Chem. Eng. Sci., 123 (2015), pp. 220-230, 10.1016/j.ces.2014.10.020

ArticleDownload PDFView Record in ScopusGoogle Scholar

[41]

M. Friedle, G.B. Marin, G.J. Heynderickx

Operational range of a gas-solid vortex unit

Powder Technol., 338 (2018), pp. 702-715, 10.1016/j.powtec.2018.07.062

ArticleDownload PDFView Record in ScopusGoogle Scholar